CrossMark

OGLE-2013-BLG-0911Lb: A Secondary on the Brown-dwarf Planet Boundary around an M Dwarf

Shota Miyazaki[1,68], Takahiro Sumi[1,68], David P. Bennett[2,3,68], Andrzej Udalski[4,69], Yossi Shvartzvald[5,70], Rachel Street[6,71], Valerio Bozza[7,8,72], Jennifer C. Yee[9,73], Ian A. Bond[10], Nicholas Rattenbury[11], Naoki Koshimoto[1], Daisuke Suzuki[12], Akihiko Fukui[13,14],

and

F. Abe[15], A. Bhattacharya[2,3], R. Barry[3], M. Donachie[11], H. Fujii[15], Y. Hirao[1], Y. Itow[15], Y. Kamei[15], I. Kondo[1], M. C. A. Li[11], C. H. Ling[10], Y. Matsubara[15], T. Matsuo[1], Y. Muraki[15], M. Nagakane[1], K. Ohnishi[16], C. Ranc[3], T. Saito[17], A. Sharan[11], H. Shibai[1], H. Suematsu[1], D. J. Sullivan[18], P. J. Tristram[19], T. Yamakawa[15], A. Yonehara[20]
(MOA collaboration),
J. Skowron[4], R. Poleski[21], P. Mróz[4,22], M. K. Szymański[4], I. Soszyński[4], P. Pietrukowicz[4], S. Kozłowski[4], K. Ulaczyk[4], Ł. Wyrzykowski[4]
(OGLE collaboration),
Matan Friedmann[23], Shai Kaspi[23], Dan Maoz[23]
(Wise team),
M. Albrow[24], G. Christie[25], D. L. DePoy[26], A. Gal-Yam[27], A. Gould[28,29,30], C.-U. Lee[31,32], I. Manulis[27], J. McCormick[33], T. Natusch[25,34], H. Ngan[25], R. W. Pogge[35,36], I. Porritt[37]
(μFUN),
Y. Tsapras[38], E. Bachelet[6,39], M. P. G. Hundertmark[38], M. Dominik[40], D. M. Bramich[41,42,43], A. Cassan[44], R. Figuera Jaimes[40,45], K. Horne[40], R. Schmidt[38], C. Snodgrass[46], J. Wambsganss[38], I. A. Steele[47], J. Menzies[48], S. Mao[49,50,51]
(RoboNet),
and
U. G. Jørgensen[52], M. J. Burgdorf[53], S. Ciceri[30], S. Calchi Novati[54], G. D'Ago[7,8,55], D. F. Evans[56], T. C. Hinse[57], N. Kains[51], E. Kerins[51], H. Korhonen[58], L. Mancini[30], A. Popovas[52], M. Rabus[59], S. Rahvar[60], G. Scarpetta[61,62], J. Skottfelt[52,63], J. Southworth[56], G. D'Ago[64], N. Peixinho[65,66], and P. Verma[67]
(MiNDSTEp)

[1] Department of Earth and Space Science, Graduate School of Science, Osaka University, 1-1 Machikaneyama, Toyonaka, Osaka 560-0043, Japan
[2] Department of Physics, University of Notre Dame, Notre Dame, IN 46556, USA
[3] Laboratory for Exoplanets and Stellar Astrophysics, NASA/Goddard Space Flight Center, Greenbelt, MD 20771, USA
[4] Warsaw University Observatory, Al. Ujazdowskie 4, 00-478 Warszawa, Poland
[5] IPAC, Mail Code 100-22, Caltech, 1200 East California Boulevard, Pasadena, CA 91125, USA
[6] Las Cumbres Observatory Global Telescope Network, 6740 Cortona Drive, Suite 102, Goleta, CA 93117, USA
[7] Dipartimento di Fisica "E.R. Caianiello," Universitá di Salerno, Via Giovanni Paolo II 132, I-84084, Fisciano, Italy
[8] Istituto Nazionale di Fisica Nucleare, Sezione di Napoli, Napoli, Italy
[9] Center for Astrophysics|Harvard & Smithsonian, 60 Garden Street, Cambridge, MA 02138, USA
[10] Institute of Information and Mathematical Sciences, Massey University, Private Bag 102-904, North Shore Mail Centre, Auckland, New Zealand
[11] Department of Physics, University of Auckland, Private Bag 92019, Auckland, New Zealand
[12] Institute of Space and Astronautical Science, Japan Aerospace Exploration Agency, 3-1-1 Yoshinodai, Chuo, Sagamihara, Kanagawa 252-5210, Japan
[13] Department of Earth and Planetary Science, Graduate School of Science, The University of Tokyo, 7-3-1 Hongo, Bunkyo-ku, Tokyo 113-0033, Japan
[14] Instituto de Astrofísica de Canarias, Vía Láctea s/n, E-38205 La Laguna, Tenerife, Spain
[15] Institute for Space-Earth Environmental Research, Nagoya University, Nagoya 464-8601, Japan
[16] Nagano National College of Technology, Nagano 381-8550, Japan
[17] Tokyo Metropolitan College of Industrial Technology, Tokyo 116-8523, Japan
[18] School of Chemical and Physical Sciences, Victoria University, Wellington, New Zealand
[19] University of Canterbury Mt. John Observatory, P.O. Box 56, Lake Tekapo 8770, New Zealand
[20] Department of Physics, Faculty of Science, Kyoto Sangyo University, Kyoto 603-8555, Japan
[21] Department of Astronomy, Ohio State University, 140 W. 18th Avenue, Columbus, OH 43210, USA
[22] Division of Physics, Mathematics, and Astronomy, California Institute of Technology, Pasadena, CA 91125, USA
[23] School of Physics and Astronomy and Wise Observatory, Tel-Aviv University, Tel-Aviv 6997801, Israel
[24] Department of Physics and Astronomy, University of Canterbury, Private Bag 4800, Christchurch, New Zealand
[25] Auckland Observatory, Auckland, New Zealand
[26] Department of Physics and Astronomy, Texas A&M University, College Station, TX 77843-4242, USA
[27] Department of Particle Physics and Astrophysics, Weizmann Institute of Science, 76100 Rehovot, Israel
[28] Department of Astronomy, Ohio State University, 140 West 18th Avenue, Columbus, OH 43210, USA
[29] Korea Astronomy and Space Science Institute, Daejon 34055, Republic of Republic of Korea
[30] Max Planck Institute for Astronomy, Königstuhl 17, D-69117 Heidelberg, Germany
[31] Korea Astronomy and Space Science Institute, 776 Daedukdae-ro, Daejeon, Republic of Korea
[32] University of Science and Technology, Korea, (UST), 217 Gajeong-ro Yuseong-gu, Daejeon 34113, Republic of Korea
[33] Farm Cove Observatory, Centre for Backyard Astrophysics, Pakuranga, Auckland, New Zealand
[34] Institute for Radio Astronomy and Space Research (IRASR), AUT University, Auckland, New Zealand
[35] Department of Astronomy, The Ohio State University, 140 W 18th Avenue, Columbus, OH 43210, USA
[36] Center for Cosmology & AstroParticle Physics, The Ohio State University, 191 West Woodruff Avenue, Columbus, OH 43210, USA

[37] Turitea Observatory, Palmerston North, New Zealand
[38] Astronomisches Rechen-Institut, Zentrum für Astronomie der Universität Heidelberg (ZAH), D-69120 Heidelberg, Germany
[39] Qatar Environment and Energy Research Institute(QEERI), HBKU, Qatar Foundation, Doha, Qatar
[40] Centre for Exoplanet Science, SUPA School of Physics & Astronomy, University of St Andrews, North Haugh, St Andrews, KY16 9SS, UK
[41] Center for Space Science, NYUAD Institute, New York University Abu Dhabi, P.O. Box 129188, Saadiyat Island, Abu Dhabi, UAE
[42] Center for Astro, Particle and Planetary Physics, New York University Abu Dhabi, P.O. Box 129188, Saadiyat Island, Abu Dhabi, UAE
[43] Division of Engineering, New York University Abu Dhabi, P.O. Box 129188, Saadiyat Island, Abu Dhabi, UAE
[44] Institut dAstrophysique de Paris, Sorbonne Université, CNRS, UMR 7095, 98 bis bd Arago, F-75014 Paris, France
[45] European Southern Observatory, Karl-Schwarzschild-Str. 2, D-85748 Garching bei München, Germany
[46] Institute for Astronomy, University of Edinburgh, Royal Observatory, Blackford Hill, Edinburgh, EH9 3HJ, UK
[47] Astrophysics Research Institute, Liverpool John Moores University, Liverpool CH41 1LD, UK
[48] South African Astronomical Observatory, P.O. Box 9, Observatory 7935, South Africa
[49] Physics Department and Tsinghua Centre for Astrophysics, Tsinghua University, Beijing 100084, People's Republic of China
[50] National Astronomical Observatories, Chinese Academy of Sciences, 20A Datun Road, Chaoyang District, Beijing 100012, People's Republic of China
[51] Jodrell Bank Centre for Astrophysics, School of Physics and Astronomy, The University of Manchester, Oxford Road, Manchester M13 9PL, UK
[52] Niels Bohr Institute & Centre for Star and Planet Formation, University of Copenhagen, Øster Voldgade 5, DK-1350 Copenhagen, Denmark
[53] Meteorologisches Institut, Universität Hamburg, Bundesstraße 55, D-20146 Hamburg, Germany
[54] IPAC, Mail Code 100-22, Caltech, 1200 E. California Boulevard, Pasadena, CA 91125, USA
[55] Spitzer Science Center, MS 220-6, California Institute of Technology, Pasadena, CA, USA
[56] Astrophysics Group, Keele University, Staffordshire, ST5 5BG, UK
[57] Chungnam National University, Department of Astronomy and Space Science, Daejeon 34134, Republic of Korea
[58] Dark Cosmology Centre, Niels Bohr Institute, University of Copenhagen, Juliane Maries Vej 30, DK-2100 Copenhagen, Denmark
[59] Instituto de Astrofísica, Facultad de Física, Pontificia Universidad Católica de Chile, Av. Vicuña Mackenna 4860, 7820436 Macul, Santiago, Chile
[60] Department of Physics, Sharif University of Technology, P.O. Box 11155-9161 Tehran, Iran
[61] Dipartimento di Fisica "E.R. Caianiello," Università di Salerno, Via Giovanni Paolo II 132, Fisciano, I-84084, Italy
[62] International Institute for Advanced Scientific Studies (IIASS), Via G. Pellegrino 19, I-84019 Vietri sul Mare (SA), Italy
[63] Centre for Electronic Imaging, Department of Physical Sciences, The Open University, Milton Keynes, MK7 6AA, UK
[64] Instituto de Astrofisica, Facultad de Fisica, Pontificia Universidad Catolica de Chile, Av. Vicuna Mackenna 4860,7820436 Macul, Santiago, Chile
[65] CITEUCCentre for Earth and Space Science Research of the University of Coimbra, Observatório Geofísico e Astronómico da U.C., 3030-004 Coimbra, Portugal
[66] Unidad de Astronomía, Fac. de Cs. Básicas, Universidad de Antofagasta, Avda U. de Antofagasta 02800, Antofagasta, Chile
[67] Istituto Internazionale per gli Alti Studi Scientifici (IIASS), Via G. Pellegrino 19, I-84019 Vietri sul Mare (SA), Italy
Received 2019 October 17; revised 2019 December 18; accepted 2019 December 19; published 2020 January 31

Abstract

We present the analysis of the binary-lens microlensing event OGLE-2013-BLG-0911. The best-fit solutions indicate the binary mass ratio of $q \simeq 0.03$, which differs from that reported in Shvartzvald et al. The event suffers from the well-known close/wide degeneracy, resulting in two groups of solutions for the projected separation normalized by the Einstein radius of $s \sim 0.15$ or $s \sim 7$. The finite source and the parallax observations allow us to measure the lens physical parameters. The lens system is an M dwarf orbited by a massive Jupiter companion at very close ($M_{\rm host} = 0.30^{+0.08}_{-0.06} M_\odot$, $M_{\rm comp} = 10.1^{+2.9}_{-2.2} M_{\rm Jup}$, $a_{\rm exp} = 0.40^{+0.05}_{-0.04}$ au) or wide ($M_{\rm host} = 0.28^{+0.10}_{-0.08} M_\odot$, $M_{\rm comp} = 9.9^{+3.8}_{-3.5} M_{\rm Jup}$, $a_{\rm exp} = 18.0^{+3.2}_{-3.2}$ au) separation. Although the mass ratio is slightly above the planet-brown dwarf (BD) mass-ratio boundary of $q = 0.03$, which is generally used, the median physical mass of the companion is slightly below the planet-BD mass boundary of $13 M_{\rm Jup}$. It is likely that the formation mechanisms for BDs and planets are different and the objects near the boundaries could have been formed by either mechanism. It is important to probe the distribution of such companions with masses of $\sim 13 M_{\rm Jup}$ in order to statistically constrain the formation theories for both BDs and massive planets. In particular, the microlensing method is able to probe the distribution around low-mass M dwarfs and even BDs, which is challenging for other exoplanet detection methods.

Unified Astronomy Thesaurus concepts: Gravitational microlensing (672); Exoplanet astronomy (486); Brown dwarfs (185); Exoplanet systems (484); Exoplanets (498); Extrasolar gas giants (509); Exoplanet detection methods (489); M dwarf stars (982)

1. Introduction

Brown dwarfs (BDs) have masses of $13–75 M_{\rm Jup}$, as they are intermediate between the masses of main-sequence stars and planets (Burrows et al. 1993). Although the existence of BDs was first proposed in Kumar (1962), there had been no observational evidence for BDs until 1995 (Nakajima et al. 1995) owing to their low luminosities and temperatures. To date, more than 10,000 field BDs have been discovered by several survey groups, which are summarized in Table 1 of Carnero Rosell et al. (2019). Most current theories predict that field BDs are formed in a fashion similar to that of main-sequence stars, through direct gravitational collapse and turbulent fragmentation of molecular clouds (Luhman 2012). These theories are observationally supported. For example, André et al. (2012) found self-gravitating dense clumps of gases and dust with mass $0.015–0.03 M_\odot$, which are similar to those of low-mass BDs. On the other hand, the core accretion mechanism (Mordasini et al. 2009; Tanigawa & Tanaka 2016) and that of gravitational instability (Boss 1997, 2001) are also able to produce companions of BD masses in protoplanetary disks. Radial velocity (RV) surveys have revealed that the frequency of BD companions with orbital radii less than ~ 3 au around main-sequence stars is relatively lower than that of

---

[68] MOA collaboration.
[69] OGLE collaboration.
[70] Wise team.
[71] RoboNet.
[72] MiNDSTEp.
[73] μFUN.
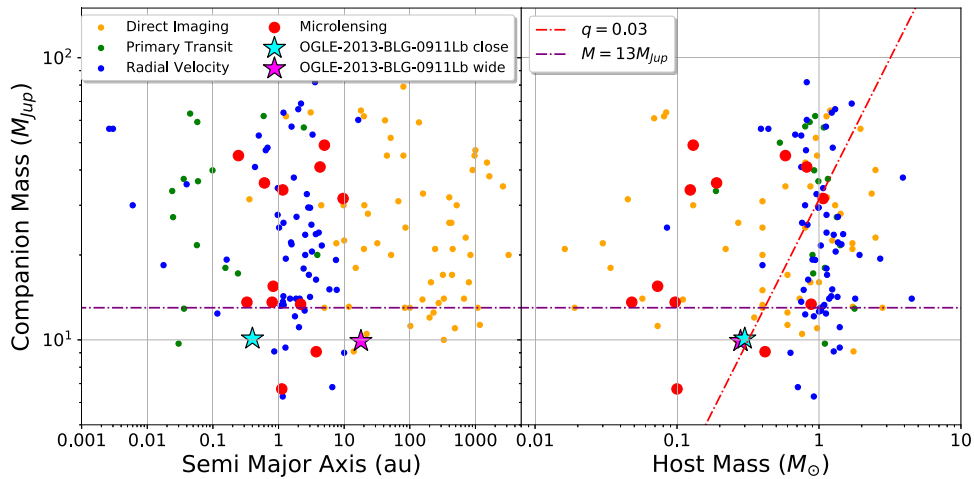
Figure 1. Distributions of discovered BD/massive-planet companions ($5M_{\mathrm{Jup}} \leqslant M \leqslant 75M_{\mathrm{Jup}}$) obtained from http://exoplanet.eu, in which the vertical axis shows the companion masses. The horizontal axes for the left and right panels indicate the semimajor axes and host masses, respectively. The yellow, green, blue, and red points indicate the BD/massive-planet companions discovered by Imaging, Transit, Radial Velocity, and Microlensing methods, respectively. The two solutions for OGLE-2013-BLG-0911Lb are represented as stars.

stellar and planetary-mass companions (Marcy & Butler 2000; Grether & Lineweaver 2006; Johnson et al. 2010), the so-called "BD desert." It is likely that this BD deficit is because of differences between the formation mechanisms of companions with planetary mass and stellar mass. However, it is not yet clear if the BD-mass companions formed like planets in the protoplanetary disk, formed as binary stars in the molecular cloud, or were captured by the primary stars. Some theories have suggested that the BD desert might be an outcome of the interaction between massive companions and protoplanetary disks and/or of tidal evolution (Armitage & Bonnell 2002; Matzner & Levin 2005; Duchêne & Kraus 2013).

Gravitational microlensing (Mao & Paczynski 1991) surveys have probed the distribution of the outer planetary systems beyond the snow line (Hayashi 1981), where ice-dominated solid materials are rich, leading to efficient formation of gas-giant planets according to the core accretion theory (Lissauer 1993; Pollack et al. 1996). Because microlensing does not depend on the luminosity of the host star, the technique is sensitive to companions to low-mass objects such as late M dwarfs or even BDs. Furthermore, the host and any companions can still be inferred at distances all the way to the Galactic bulge. In contrast, the RV and transit (Borucki et al. 2010) methods, which have discovered the bulk of currently known exoplanets and BDs orbiting around hosts, have only a sensitivity to companions relatively close to hosts and whose hosts are sufficiently bright. Figure 1 shows the distribution of discovered BD/massive-planet companions around main-sequence stars and BDs. The RV (blue dots) and transit (green dots) methods have discovered a lot of the companions around $1\,M_\odot$ stars but only a few around low-mass stars below $0.5\,M_\odot$. This would be caused by an observational bias due to the faintness of low-mass stars in the visible wavelength range. The direct imaging (orange dots) method has detected the companions around hosts with masses of 0.01–$3\,M_\odot$, but it could not have resolved the companions with relatively short orbital radii. On the other hand, microlensing (red dots) has discovered BD/massive-planet companions around hosts with masses of ~ 0.05–$1M_\odot$ with orbital radii of ~ 0.3–10 au (e.g., Ranc et al. 2015; Han et al. 2017; Ryu et al.

2018), which are complementary to other detection methods. Gaudi (2002) estimated that more than 25% of BD companions with separations ~ 1–10 au would be detected by present microlensing surveys. According to the standard core accretion theory, massive planets as well as BDs are more difficult to form around low-mass M dwarfs than solar-type stars owing to low disk surface densities (Ida & Lin 2005) and long timescales (Laughlin et al. 2004). It is possible to constrain the BD formation mechanism around late M dwarfs from a statistical analysis of microlensing results in the BD-mass regime, which can be compared to the lack of close-in BD companions around solar-type stars found by RV observations.

Shvartzvald et al. (2016, hereafter S16) conducted a statistical analysis of the first four seasons of a "second-generation" microlensing survey (Gaudi et al. 2009), which consisted of the observations by the Optical Gravitational Lensing Experiment (OGLE; Udalski et al. 1994) collaboration, the Microlensing Observations in Astrophysics (MOA; Bond et al. 2001; Sumi et al. 2003) collaboration, and the Wise team (Shvartzvald & Maoz 2012). They analyzed 224 microlensing events and found 29 "anomalous" events, implying the presence of a companion to the lens host. They performed an automated coarse grid search for light-curve modelings rather than a detailed modeling of individual events for their statistical study. Finally, they derived the planet (binary) frequency distribution as a function of companion-to-host mass ratio q and found a possible deficit at $q \sim 10^{-2}$. However, it is worthwhile to conduct a detailed analysis of individual "planetary candidate" in their sample, for which there are not any models in the literature. For example, they reported that OGLE-2013-BLG-0911 has a planetary mass-ratio of $q \approx 3 \times 10^{-4}$, but we found new preferred solutions with a less extreme mass ratio, $q \approx 3 \times 10^{-2}$.

Here, we present the analysis of a high-magnification (maximum magnification of $A_{\max} \sim 220$) microlensing event, OGLE-2013-BLG-0911. The "anomaly", due to a companion to the lens star, was clearly detected near the peak of the light curve. We present the observations and data sets of the event in Section 2. Our light-curve analysis is described in Section 3. In Section 4, we present our analysis of the source

properties. The physical parameters of the lens system are described in Section 5. We summarize and discuss the results in Section 6.

2. Observation and Data Sets

2.1. Observation

The microlensing event OGLE-2013-BLG-0911 was discovered and alerted as a microlensing candidate on 2013 June 3 UT 21:51 by the fourth phase of the OGLE collaboration (OGLE-IV; Udalski et al. 2015). OGLE-IV[74] is conducting a microlensing exoplanet search toward the Galactic bulge using the 1.3 m Warsaw telescope of Las Campanas Observatory in Chile with a wide total field of view (FOV) of 1.4 deg^2. The OGLE observations were conducted using the standard I- and near-standard V-band filters. The second phase of the MOA collaboration[75] (MOA-II; Bond et al. 2017) is also carrying out a microlensing survey toward the Galactic bulge using the 1.8 m MOA-II telescope with a 2.2deg^2 FOV CCD camera (MOA-cam3; Sako et al. 2008) at Mount John Observatory in New Zealand. Thanks to its wide FOV, the MOA collaboration is observing bulge stars with a cadence of 15–90 minutes every day depending on the field. The MOA survey independently discovered and issued an alert for the event as MOA-2013-BLG-551. The MOA observations were conducted using a custom wide-band filter, "MOA–Red," which corresponds approximately to the combination of the standard I and R filters. The Wise[76] team also conducted a microlensing survey from 2010 to 2015 and monitored a field of 8 deg^2 within the observational footprints of both OGLE and MOA (Shvartzvald & Maoz 2012). They observed using the 1 m Wise telescope at Wise Observatory in Israel with a 1 deg^2 FOV LAIWO camera (Gorbikov et al. 2010) and the cadence for each of the eight Wise fields was ∼30 minutes.

The event was located at (R.A., decl.)$_{J2000}$ = (17:55:31.98, −29:15:13.8) or Galactic coordinates (l, b) = (0°.84, −2°.02). Real-time analysis predicted the event would reach high peak magnification during which the sensitivity to low-mass companions is high (Griest & Safizadeh 1998; Rattenbury et al. 2002). Follow-up observations during the period of high magnification were encouraged to capture short planetary signals. Consequently, in addition to the OGLE and MOA survey observations, the light curve was densely observed by several follow-up groups: Microlensing Follow Up Network (μFUN; Gould et al. 2006), Microlensing Network for the Detection of Small Terrestrial Exoplanets (MiNDSTEp; Dominik et al. 2010), and RoboNet (Tsapras et al. 2009; Dominik et al. 2019). Hereafter, we refer this event as OGLE-2013-BLG-0911.

2.2. Data Reduction

All of the data sets of OGLE-2013-BLG-0911 are summarized in Table 1. Most photometric pipelines use the Difference Image Analysis (DIA; Alard & Lupton 1998; Alard 2000) technique, which is very effective in high stellar density fields such as those toward the Galactic bulge. The MOA and μFUN CTIO data were reduced with the MOA implementation of the DIA method (Bond et al. 2001, 2017).

The OGLE data were reduced by OGLE's DIA pipeline (Wozniak 2000). The Wise data were reduced using the pySIS DIA software (Albrow et al. 2009). The other μFUN data and MiNDSTEp data were reduced by DoPhot (Schechter et al. 1993) and DanDIA (Bramich 2008; Bramich et al. 2013). RoboNet data were reduced using a customized version of the DanDIA pipeline (Bramich 2008).

It is known that the nominal photometric error bars given by each photometric pipeline are potentially underestimated in high stellar density fields toward the bulge. Therefore, we empirically renormalized the error bars for each data set following procedure of Bennett et al. (2008) and Yee et al. (2012), i.e.,

$$\sigma_i' = k\sqrt{\sigma_i^2 + e_{\min}^2}, \qquad (1)$$

where σ_i' and σ_i represent the renormalized errors and the original errors given by the pipelines, respectively. The parameters k and $e_{\min}$ are the coefficients for the error renormalization. Here, $e_{\min}$ represents the systematic errors when the source flux is significantly magnified. We added 0.3% in quadrature to each error, i.e., $e_{\min} = 0.003$, and then calculated k values in order to achieve a value of $\chi^2/\mathrm{dof} = 1$ for each data set (Bennett et al. 2014; Skowron et al. 2016). We list the renormalization coefficients k in Table 1 along with the number of used data points N_{use}. We confirmed that the final best-fit model is consistent with the preliminary best-fit model found using the data sets before the error renormalization.

3. Light-curve Modeling

Here, we present the light-curve modeling for OGLE-2013-BLG-0911. Figure 2 represents the light curve of OGLE-2013-BLG-0911. The main anomalous feature can be seen between $6536.8 < \mathrm{HJD} - 245000 < 6537.6$. A standard single-lens single-source (1L1S) model fits the data worse than a binary-lens single-source (2L1S) model by $\Delta\chi^2 > 3500$. In following sections, we present the details of the light-curve modeling for OGLE-2013-BLG-0911. In Table 2, we summarize the comparisons of the χ^2, number of fitting parameters, and Bayesian information criterion (BIC) between the microlensing models we examined.

3.1. Model Description

Assuming a single source star, the observed flux at any given time in a microlensing event, $F_{\mathrm{obs}}(t)$, can be modeled by the following equation:

$$F_{\mathrm{obs}}(t) = A(t)F_{\mathrm{s}} + F_{\mathrm{b}}, \qquad (2)$$

where $A(t)$ is the magnification of the source flux, F_{s} is the unmagnified source flux, and F_{b} is the blend flux. We note that F_{s} and F_{b} can be, during the fitting process, solved analytically by the linear Equation (2) at given $A(t)$. For a standard 1L1S model, there are four parameters that describe the light-curve features (Paczynski 1986): (1) the time of the source approaching closest to the lens center of mass, t_0, (2) the impact parameter, u_0, in units of the angular Einstein radius, θ_{E}, (3) the Einstein radius crossing time, t_{E}, and (4) the source angular radius, ρ, in units of θ_{E}. The measurement of ρ is important because it leads to a determination of θ_{E}, which is

---

[74] http://ogle.astrouw.edu.pl/ogle4/ews/ews.html
[75] https://www.massey.ac.nz/~iabond/moa/alerts/
[76] http://wise-obs.tau.ac.il/~wingspan/

Table 1
Data Sets for OGLE-2013-BLG-0911

Site	Telescope	Collaboration	Label	Filter	N_{use}	k^a
Mount John Observatory	MOA-II 1.8 m	MOA	MOA	Red	8761	1.055
Las Campanas Observatory	Warsaw 1.3 m	OGLE	OGLE	I	6895	1.480
Las Campanas Observatory	Warsaw 1.3 m	OGLE	OGLE	V	78	1.344
Florence and George Wise Observatory	Wise 1 m	Wise	Wise1m	I	253	0.947
Cerro Tololo-Inter-American Observatory (CTIO)	SMARTS 1.3 m	μFUN	CT13	I	189	1.230
Cerro Tololo-Inter-American Observatory (CTIO)	SMARTS 1.3 m	μFUN	CT13	V	35	1.182
Farm Cove Observatory	Farm Cove 0.36 m	μFUN	FCO	Unfiltered	55	2.146
Weizmann Institute of Science, Marty S. Kraar Observatory	Weizmann 16 inch	μFUN	WIS	I	17	1.140
Haleakala Observatory	Faulkes North 2.0 m	RoboNet	FTN	i'	27	2.181
Siding Spring Observatory (SSO)	LCO 1.0 m, Dome A	RoboNet	cojA	i'	31	1.920
Cerro Tololo Inter-American Observatory (CTIO)	LCO 1.0 m, Dome B	RoboNet	lscB	i'	51	1.311
Cerro Tololo Inter-American Observatory (CTIO)	LCO 1.0 m, Dome C	RoboNet	lscC	i'	71	2.315
South African Astronomical Observatory (SAAO)	LCO 1.0 m, Dome A	RoboNet	cptA	i'	32	0.559
South African Astronomical Observatory (SAAO)	LCO 1.0 m, Dome B	RoboNet	cptB	i'	8	0.497
ESO's La Silla Observatory	Danish 1.54 m	MiNDSTEp	Dan	I	76	2.087
Salerno University Observatory	Salerno 0.36 m	MiNDSTEp	Sal	I	20	1.607

Notes. The WIS, Sal, and lscC data are binned for 0.01 days.
[a] The coefficient for error renormalization, see the text.

needed for the determination of the the mass–distance relation of the lens system.

In our fitting process, we used a Markov Chain Monte Carlo (MCMC) method (Verde et al. 2003) combined with our implementation of the inverse ray-shooting method (Bennett & Rhie 1996; Bennett 2010) in order to find the best-fit model and estimate the parameter uncertainties from MCMC stationary distribution for each parameter. Linear limb-darkening models were used to describe the source star(s) in this work. From the measurement of the intrinsic source color of $(V − I)_{s,0} = 0.71$ described in Section 4, we assumed an effective temperature $T_{eff} = 5750$ K (González Hernández & Bonifacio 2009), surface gravity $\log g = 4.5$, and metallicity $\log[M/H] = 0$. According to the ATLAS model of Claret & Bloemen (2011), we selected limb-darkening coefficients of $u_{Red} = 0.5900$, $u_I = 0.5493$, $u_V = 0.7107$. Here, u_{Red} for the MOA–Red band is estimated as the mean of u_I and u_R, and the R-band coefficient $u_R = 0.6345$ is used for an unfiltered band.

3.2. Binary-lens (2L1S) Model

For a standard 2L1S model, there are three additional parameters: (1) the lens mass ratio between the host and a companion, q, (2) the projected binary separation in unit of the Einstein radius, s, and (3) the angle between the source trajectory and the binary-lens axis, α. Here, we introduce two fitting parameters t_c and u_c, for wide ($s > 1$) models. If $s > 1$, the system center in our numerical code is offset from the binary center of mass by

$$\Delta(x, y) = \left[\frac{q}{1+q}\left(\frac{1}{s} - s\right), 0 \right]$$

where (x, y) are the parallel and vertical coordinate axes to the binary-lens axis on the lens plane (Skowron et al. 2011), and then we define the time of the source approaching closest to the "system center" and the impact parameter in units of the angular Einstein radius as t_c and u_c, respectively.

3.2.1. Static Models

At first, we explored the 2L1S interpretation to explain the anomalous features of the light curve. In modeling 2L1S microlensing light curves, it is common to encounter situations where different physical models explain the observed data equally well, e.g., the close/wide degeneracy (Griest & Safizadeh 1998; Dominik 1999) and the planet/binary degeneracy (Choi et al. 2012; Miyazaki et al. 2018), where different combinations of the microlensing parameters can generate morphologically similar light curves. Therefore, we should thoroughly investigate the multi-dimensional parameter space to find the global preferred model solution. We conducted a detailed grid search over the (q, s, α) parameter space where the magnification pattern strongly depends on these three parameters. The search ranges of q, s, and α are $-1 < \log s < 1$, $-4.5 < \log q < 0$, and $0 < \alpha < 2\pi$ with 40 grid points, respectively, and thus, the total number of grid points is $40 \times 40 \times 40 = 64,000$. We conducted the grid search analysis following the same procedure written in Miyazaki et al. (2018). Figure 3 shows the map of the minimum $\Delta\chi^2$ in each s–q grid from the grid search. In Figure 3, we found two possible local minima around ($\log q$, $\log s$) $\sim (-1.8, -0.75)$ and $\sim (-1.8, 0.75)$, which is caused by the close/wide degeneracy. After refining all possible solutions, we found the best-fit 2L1S close ($s < 1$) and wide ($s > 1$) models with $q \sim 0.03$, where the χ^2 difference between them is only $\Delta\chi^2 = 4.9$. As seen in Figure 2, the 2L1S model with $q \sim 0.03$ provide good fits to the anomalous features around the top of the light curve. We also show the model light curve of 2L1S with $q \sim 10^{-4}$ in Figure 2, and it does not fit the light-curve anomaly well.

S16 included this event in their statistical analysis as a planetary microlensing event, using a mass ratio of $q \sim 10^{-4}$ for this event. However, our reanalysis found that the static 2L1S models with $q \sim 10^{-2}$ are preferred over the model with $q \sim 10^{-4}$ by $\Delta\chi^2 > 700$. The reason for this oversight is that models with $q \sim 10^{-2}$ are outside of the range of their grid search of $-6 < \log q < 0$ and $0.3 < s < 3$, and the search for the best-fit model outside of this range by refining model parameters found by their grid search was not conducted.
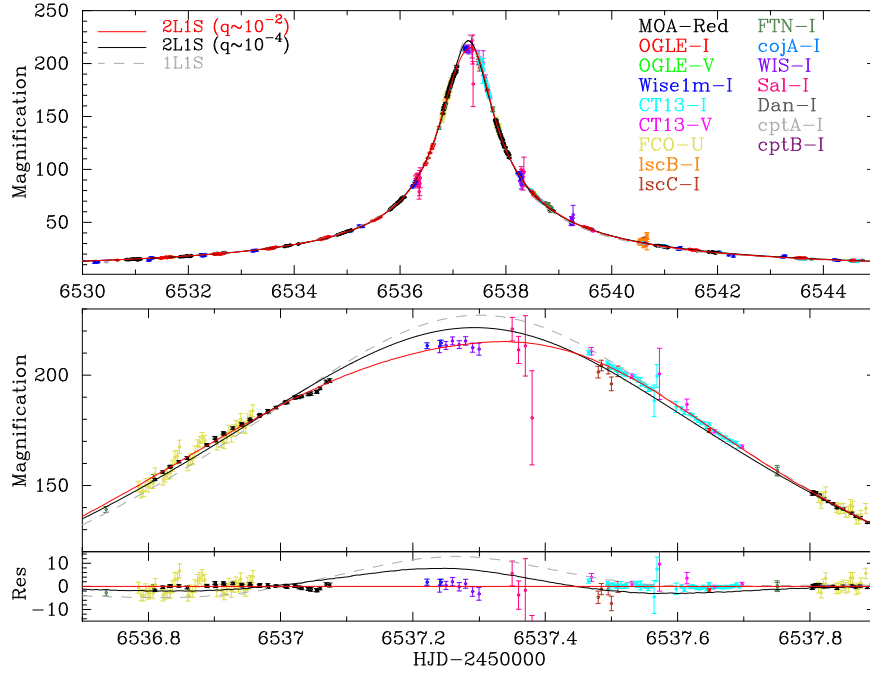
Figure 2. (Top panel) Light curve of OGLE-2013-BLG-0911. Each color on the data point corresponds to each instrument, shown on the right. The error bars are renormalized following Equation (1). The solid red, solid black, and dashed gray curves represent the static 2L1S with $q \sim 10^{-2}$, 2L1S with $q \sim 10^{-4}$, and 1L1S models, respectively. (Middle panel) A zoom-in around the peak. (Bottom panel) Residuals of the zoom-in light curve from the model of 2L1S with $q \sim 10^{-2}$.

Another difference from S16 is that we used re-reduced MOA and OGLE light curves and included all of the follow-up data sets. However, we confirmed that the 2L1S models with $q \sim 10^{-4}$ are disfavored relative to the models with $q \sim 10^{-2}$ by $\Delta\chi^2 > 300$ even if we used the survey data, MOA, OGLE, and Wise1m. Therefore, note that the survey data were sufficient to identify the new solutions.

3.2.2. Parallax Effects

Although the best-fit static models provide good fits to the main anomaly features around the peak of the light curve, we found that, overall, the light curve slightly deviates from the static models. The event OGLE-2013-BLG-0911 has $t_E \sim 90$ days and had continued throughout the bulk of the bulge season, which implies that the light curve could be affected by additional high-order microlensing effects.

It is known that the orbital acceleration of Earth causes a parallax effect (Gould 1992, 2004; Smith et al. 2003). This can be described by the microlensing parallax vector $\boldsymbol{\pi}_E = (\pi_{E,N}, \pi_{E,E})$. Here, $\pi_{E,N}$ and $\pi_{E,E}$ denote the north and east components of $\boldsymbol{\pi}_E$ projected to the sky plane in equatorial coordinates. The direction of $\boldsymbol{\pi}_E$ is defined so as to be identical to that of $\boldsymbol{\mu}_{rel,G}$, which is the geocentric lens-source relative proper motion projected to the sky plane at a reference time t_{fix}, and the amplitude of $\boldsymbol{\pi}_E$ is $\pi_E = au/\tilde{r}_E$ where $\tilde{r}_E$ is the Einstein radius projected inversely to the observer plane. We took a reference time $t_{fix} = 6537.3$ days for this event. The measurement of $\boldsymbol{\pi}_E$ enables constraints to be placed on the relation between the lens mass M_L and distance D_L (Gould 2000; Bennett 2008). For Galactic bulge source events, models with $(u_0, \alpha, \pi_{E,N})$ and $-(u_0, \alpha, \pi_{E,N})$ can yield very similar light curves (Skowron et al. 2011). This is reflected as a pair of the symmetric source trajectories to the binary and is sometimes referred to as "ecliptic degeneracy."

Taking the parallax effect into consideration for modeling, we found that the two parallax parameters gave an improvement of $\Delta\chi^2 \sim 210$ compared to the best-fit static model. However, we also found that the best-fit parallax model does not seem to explain the long-term deviations of the light curve from the best-fit static model, as can be seen in Figure 4. This implies that there might still be other high-order microlensing effects in the light curve. Note that adding the lens orbital motion does not improve our models.

3.2.3. Xallarap Effects

Xallarap (Griest & Hu 1992; Han & Gould 1997; Poindexter et al. 2005) is the microlensing effect on the light curve induced by the source orbital motion around the source companion. The xallarap model requires seven additional fitting parameters that determine the orbital elements of the source system; the direction toward the solar system relative to the orbital plane of the source system, R.A.$_\xi$ and decl.$_\xi$; the source orbital period, P_ξ; the source orbital eccentricity and perihelion time, e_ξ and T_{peri}; the xallarap vector, $\boldsymbol{\xi}_E = (\xi_{E,N}, \xi_{E,E})$. The direction of $\boldsymbol{\xi}_E$ is similar to that of the geocentric lens-source proper motion $\boldsymbol{\mu}_{rel,G}$ and the amplitude of $\boldsymbol{\xi}_E$ is $\xi_E = a_S/\hat{r}_E$ where a_S is the semimajor axis of the source orbit and $\hat{r}_E$ is the projected Einstein radius to the source plane, i.e., $\hat{r}_E = \theta_E D_S$. Kepler's third and Newton's third laws give the following relations (Batista et al. 2009):

$$\xi_E = \frac{1\ au}{D_S \theta_E}\left(\frac{M_c}{M_\odot}\right)\left[\frac{M_\odot}{M_c + M_S}\frac{P_\xi}{1\ yr}\right]^{2/3}, \qquad (3)$$

$$M_S a_S = M_C a_C \Rightarrow a_{SC} \equiv a_S + a_C = \left(1 + \frac{M_S}{M_C}\right)a_S, \qquad (4)$$

where M_S and M_C are the masses of the source and source companion, respectively. Therefore, we can estimate the source

6

Table 2
Comparisons between Each Microlensing Model

Model			N_{param} [a]	χ^2	BIC [b]	$\Delta\chi^2$	ΔBIC
1L1S	⋯	Static	4	21027.4	21066.3	4485.1	4368.5
1L2S	⋯	Static	10	18631.0	18728.2	2088.7	2030.4
1L2S	⋯	Xallarap	12	17554.3	17670.9	1212.0	973.1
2L1S	$(s < 1)$	Static	7	17473.7	17541.7	931.4	843.9
2L1S	$(s < 1, u_0 > 0)$	Parallax	9	17262.7	17350.2	720.4	652.4
2L1S	$(s < 1, u_0 > 0)$	Xallarap	14	16587.6	16723.6	45.3	25.8
2L1S	$(s < 1, u_0 > 0)$	Parallax+Xallarap	16	16558.9	16714.4	16.6	16.6
2L2S	$(s < 1, u_0 > 0)$	Parallax+Xallarap	16	16542.3	16697.8	⋯	⋯

Notes.
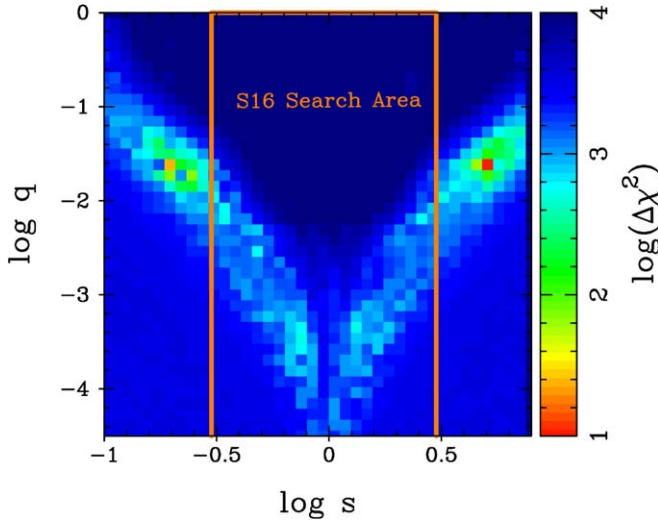[a] Number of fitting parameters.
[b] BIC.

Figure 3. Map of the minimum $\Delta\chi^2$ in each s–q grid from the grid search. The orange box corresponds to the area of the grid search analysis in Shvartzvald et al. (2016).

companion mass M_C from the xallarap measurements by assuming M_S and D_S.

Since the number of additional parameters for the xallarap effect is large, we conducted a grid search fixing (R.A.$_\xi$, decl.$_\xi$, P_ξ) in order to avoid missing any local minima. After refining all possible solutions, we found that the best-fit xallarap model is favored over the best-fit parallax model by $\Delta\chi^2 > 650$. As shown in Figure 4, including the xallarap effect produces a model that fits the long-term residuals from the best-fit static model, and it dramatically improves the χ^2 values. The best-fit orbital period of the source system is $P_\xi \sim 40$ days and is clearly different from Earth's orbital period of 365 days, which implies that the parallax and xallarap signals are clearly distinguishable. Following Equation (3), the best-fit 2L1S xallarap model indicates a source companion mass of $M_C = 0.21 M_\odot$ and a distance between two sources $a_{\mathrm{SC}} = 0.22$ au on the assumption of $M_S = 1.0 M_\odot$ and $D_S = 8$ kpc, which is a common stellar binary system in solar neighborhood (Duchêne & Kraus 2013). The best-fit ξ_E values are much smaller than 1, which means that the two sources are separated by much less than the Einstein radius. Hence, the source companion was also likely to be magnified during the event. In the following sections, we explore binary source

scenarios where both components of the binary source system are magnified by the lens.

3.3. Binary Source (1L2S) Model

When two source stars are magnified by the same single-lens, called a 1L2S event, the observed flux would be the superposition of the two magnified single-source fluxes, i.e.,

$$A(t) = \frac{A_1(t) F_{s,1} + A_2(t) F_{s,2}}{F_{s,1} + F_{s,2}} = \frac{A_1(t) + q_{F,j} A_2(t)}{1 + q_{F,j}}, \quad (5)$$

where A_i and $F_{s,i}$ represent the magnification and the baseline flux of each i-th source, and $q_{F,j} = F_{s,2}/F_{s,1}$ is the flux ratio between the two source stars in each j-th passband. For a standard (static) 1L2S model, the fitting parameters are [t_0, $t_{0,2}$, t_E, u_0, $u_{0,2}$, ρ, ρ_2, $q_{F,j}$]. Because the magnification of each source star varies independently, the total observed source color is variable during a binary source event, which happens in single-source events only if limb-darkening effects are seen during caustic crossings[77], as microlensing does not depend on wavelength. Binary source events can mimic short-term binary-lens anomalies in a light curve; therefore, it is necessary to determine whether the anomaly features are induced by the binary lens or binary source (Gaudi 1998; Jung et al. 2017a, 2017b; Shin et al. 2019).

First, we fitted the light curves with the static 1L2S model and found that it was disfavored over the static 2L1S models by $\Delta\chi^2 > 1100$. In Section 3.2.3, we found an asymmetric distortion in the light curves that can be explained by the xallarap effect (i.e., source orbital effect). Thus, we also explored 1L2S models with source orbital motion. The trajectories of two sources can be estimated by the source orbital motion from the xallarap parameters, ($\xi_{E,N}$, $\xi_{E,E}$, R.A.$_\xi$, decl.$_\xi$, P_ξ, e_ξ, T_{peri}), and Equation (3). Here, we assumed $M_S = 1\,M_\odot$ and $D_S = 8$ kpc to derive the source companion mass M_C. In Appendix B, we confirmed that the assumptions of $M_S = 1\,M_\odot$ and $D_S = 8$ kpc hardly impact the light-curve modeling. We conducted a detailed grid search of (R.A.$_\xi$, decl.$_\xi$, P_ξ) and refined all possible 1L2S solutions. We found that the best-fit 1L2S model is not preferred over the

---

[77] For point lenses, this happens only if the lens briefly transits the source (Loeb & Sasselov 1995; Gould & Welch 1996).
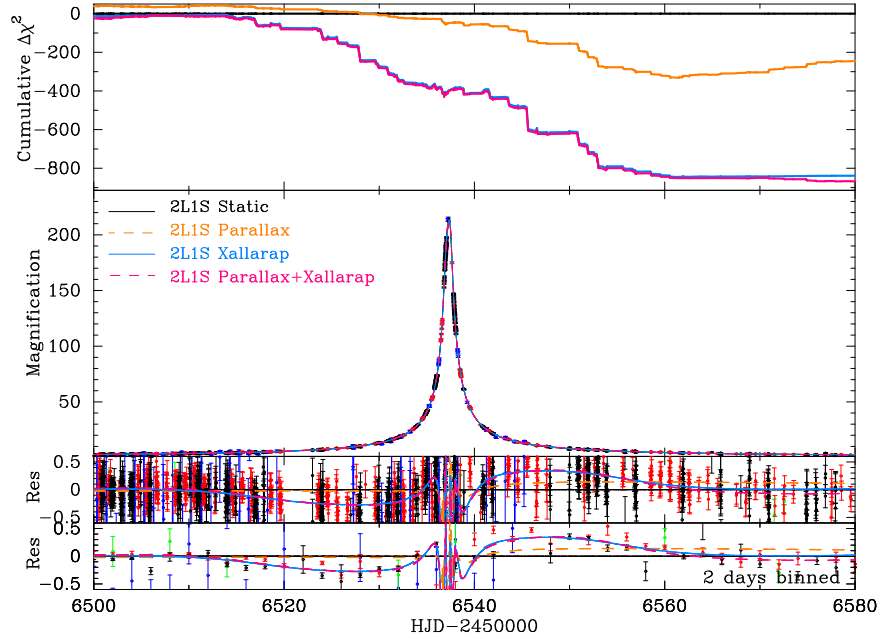
Figure 4. (Top panel) Cumulative $\Delta\chi^2$ distributions of the three 2L1S close ($u_0 > 0$) models compared to the 2L1S static model. (Second panel from the top) The light curve and models for OGLE-2013-BLG-0911. Here, we plot only MOA, OGLE, and Wise 1m light curves for clarity. (Third panel from the top) The residuals of the light curve and models from the static model. (Bottom panel) The residuals binned by 2 days.

static 2L1S models by $\Delta\chi^2 > 80$, even if we introduced the source orbital motion.

3.4. Binary-lens Binary-source (2L2S) Model

Finally, we explored the 2L2S models with source orbital motion, i.e., taking into account the flux from the source companion and the xallarap effect. Here, we adopted the flux ratio q_F estimated from M_C, which is derived from the xallarap parameters to maintain consistency. We derived the flux ratios in each band from a combination of M_C and a theoretical stellar isochrone model[78] (PARSEC; Bressan et al. 2012) for solar metallicity and a typical bulge star age of 10 Gyr. For the MOA–Red band, we derived the flux ratio from that in I- and V- bands, $q_{F,\mathrm{Red}} = q_{F,I}^{0.827} q_{F,V}^{0.173}$. This formula comes from the following color transformation that is derived by using bright stars around the event (Gould et al. 2010; Bennett et al. 2012, 2018),

$$R_{\mathrm{MOA}} - I_{\mathrm{O3}} = 0.173(V_{\mathrm{O3}} - I_{\mathrm{O3}}) + \mathrm{const} \qquad (6)$$

where R_{MOA}, I_{O3}, and V_{O3} are the magnitudes in MOA–Red, OGLE-III I-, and V-bands, respectively. For the Unfiltered passband, we used the R-band flux ratio assuming $q_{F,\mathrm{Unfiltered}} \approx q_{F,R}$.

We found the four best 2L2S models, which suffer from the close/wide degeneracy and the ecliptic degeneracy. The parameters of these models are shown in Table 3. The light curve of the best-fit 2L2S ($s < 1$, $u_0 > 0$) model is shown in Figure 5. Here, as shown in Equation (5), the light curves in each passband are different. The black, red, green, and cyan solid curves indicate the model light curves in the MOA–Red, I-, V-, and R-bands, respectively. The caustic geometry and source trajectories of the best-fit 2L2S ($s < 1$, $u_0 > 0$) model are shown in Figure 6. Here, the source companion trajectory indicates that the source companion is more strongly magnified

than the primary source. In general, such magnification differences in two sources allow us to resolve the close/wide degeneracy and the ecliptic degeneracy. However, as shown in the bottom right panel of Figure 5, where the secondary source magnification is peaked at HJD' $\sim$ 6539.55, the flux contribution is $\sim$0.01 times smaller than the primary source because the source companion is intrinsically much fainter than the primary source. Consequently, we could not resolve these degeneracies. These 2L2S models are preferred relative to the 2L1S models with parallax and xallarap effects by $\Delta\chi^2 \sim 16$ without additional fitting parameters. The fitting and physical parameters for the 2L1S and 2L2S models are almost identical each other. Therefore, it hardly affects the final results, whichever we take. Hereafter, we take the 2L2S models for the final result.

4. Source Properties

The measurement of ρ enables us to determine the angular Einstein radius $\theta_E = \theta_* / \rho$ where θ_* is the angular source radius. The angular source radius θ_* can be estimated from the extinction-free color and magnitude of the source star by using a method similar to that of Yoo et al. (2004), which adopts the centroid of the bulge red clump giants (RCG) as a reference point. Yoo et al. (2004) assumed that the source star suffers from the same extinction as that of the bulge RCG so that the extinction-free color and magnitude of the source star can be described by the following equation:

$$(V - I, I)_{S,0} = (V - I, I)_{0,\mathrm{RCG}} - \Delta(V - I, I), \qquad (7)$$

where $(V - I, I)_{0,\mathrm{RCG}} = (1.06 \pm 0.07, 14.40 \pm 0.04)$ is the extinction-free color and magnitude of the bulge RCG centroid (Bensby et al. 2011, 2013; Nataf et al. 2013) and $\Delta(V - I, I)$ are the offsets of the color and magnitude from the RCG centroid to the source star measured in the standard color–magnitude diagram (CMD).

---

[78] http://stev.oapd.inaf.it/cgi-bin/cmd

Table 3
2L2S Model Parameters

Parameters	Units	Close ($s < 1$)		Wide ($s > 1$)	
		($u_0 > 0$)	($u_0 < 0$)	($u_c > 0$)	($u_c < 0$)
$t_0 (t_c)$	HJD-2456530	$7.3128^{+0.0005}_{-0.0005}$	$7.3127^{+0.0005}_{-0.0005}$	$7.3123^{+0.0003}_{-0.0004}$	$7.3111^{+0.0005}_{-0.0006}$
t_E	day	$94.698^{+1.612}_{-1.525}$	$98.121^{+2.246}_{-0.958}$	$101.104^{+2.246}_{-1.799}$	$98.275^{+1.154}_{-1.148}$
$u_0 (u_c)$	(10^{-3})	$4.800^{+0.077}_{-0.079}$	$-4.620^{+0.041}_{-0.042}$	$4.522^{+0.086}_{-0.108}$	$-4.626^{+0.053}_{-0.053}$
q	(10^{-2})	$3.236^{+0.089}_{-0.084}$	$3.066^{+0.090}_{-0.094}$	$3.160^{+0.132}_{-0.134}$	$3.456^{+0.087}_{-0.067}$
s	$\cdots$	$0.150^{+0.002}_{-0.002}$	$0.150^{+0.002}_{-0.002}$	$6.774^{+0.101}_{-0.085}$	$7.084^{+0.074}_{-0.064}$
α	radian	$4.197^{+0.004}_{-0.004}$	$2.078^{+0.006}_{-0.008}$	$4.198^{+0.007}_{-0.007}$	$2.092^{+0.006}_{-0.005}$
ρ	(10^{-3})	$1.113^{+0.148}_{-0.118}$	$1.136^{+0.090}_{-0.144}$	$1.413^{+0.093}_{-0.295}$	$0.971^{+0.118}_{-0.085}$
$\pi_{E,N}$	$\cdots$	$0.256^{+0.044}_{-0.050}$	$0.300^{+0.027}_{-0.025}$	$0.319^{+0.039}_{-0.050}$	$0.271^{+0.032}_{-0.041}$
$\pi_{E,E}$	$\cdots$	$0.018^{+0.005}_{-0.005}$	$0.004^{+0.006}_{-0.006}$	$0.001^{+0.006}_{-0.006}$	$0.006^{+0.003}_{-0.004}$
$\zeta_{E,N}$	(10^{-3})	$-2.91^{+0.97}_{-1.01}$	$-3.13^{+1.72}_{-1.39}$	$-5.32^{+2.66}_{-1.61}$	$-2.48^{+1.28}_{-1.04}$
$\zeta_{E,E}$	(10^{-3})	$-4.31^{+0.18}_{-0.17}$	$-3.59^{+0.62}_{-0.44}$	$-3.53^{+0.45}_{-0.48}$	$-3.66^{+0.50}_{-0.33}$
R.A.$_\zeta$	degree	$-74.2^{+15.5}_{-12.2}$	$-87.4^{+15.5}_{-14.0}$	$260.9^{+13.5}_{-11.4}$	$-89.4^{+16.3}_{-16.3}$
Decl.$_\zeta$	degree	$21.8^{+6.4}_{-7.4}$	$29.8^{+2.5}_{-3.5}$	$19.7^{+2.2}_{-6.2}$	$38.0^{+7.4}_{-7.7}$
P_ξ	day	$36.67^{+0.77}_{-0.73}$	$36.28^{+0.74}_{-0.70}$	$36.82^{+0.66}_{-0.68}$	$36.51^{+0.80}_{-0.70}$
e_ξ	$\cdots$	$0.258^{+0.033}_{-0.029}$	$0.249^{+0.029}_{-0.031}$	$0.270^{+0.032}_{-0.029}$	$0.231^{+0.040}_{-0.038}$
T_{peri}	HJD-2456500	$53.14^{+1.08}_{-1.10}$	$52.75^{+0.48}_{-0.51}$	$17.31^{+0.90}_{-0.84}$	$53.69^{+0.78}_{-0.96}$
$q_{F,Red}$	(10^{-3})	$1.122^{+0.388}_{-0.330}$	$0.818^{+0.317}_{-0.254}$	$0.974^{+0.439}_{-0.298}$	$0.970^{+0.342}_{-0.261}$
$q_{F,I}$	(10^{-3})	$1.424^{+0.466}_{-0.399}$	$1.058^{+0.383}_{-0.309}$	$1.246^{+0.527}_{-0.362}$	$1.241^{+0.412}_{-0.317}$
$q_{F,V}$	(10^{-4})	$3.58^{+1.58}_{-1.29}$	$2.39^{+1.24}_{-0.93}$	$3.00^{+1.76}_{-1.12}$	$2.98^{+1.36}_{-0.99}$
$q_{F,R}$	(10^{-4})	$6.62^{+2.64}_{-2.18}$	$4.61^{+2.10}_{-1.62}$	$5.63^{+2.96}_{-1.93}$	$5.60^{+2.30}_{-1.70}$
π_E	$\cdots$	$0.257^{+0.044}_{-0.050}$	$0.300^{+0.027}_{-0.025}$	$0.319^{+0.039}_{-0.050}$	$0.271^{+0.032}_{-0.041}$
χ^2	$\cdots$	16542.2	16543.3	16542.3	16542.9
$\Delta\chi^2$	$\cdots$	$\cdots$	1.1	0.1	0.7

Note. Here, we assume $M_S = 1\,M_\odot$ and $D_S = 8$ kpc. The flux ratios q_F and parallax amplitude $\pi_E = \sqrt{\pi_{E,N}^2 + \pi_{E,E}^2}$ are not fitting parameters. All other parameters in this table are used as fitting parameters for modeling.

4.1. Photometric Source Properties

We obtained the apparent source color and magnitude of $(V - I, I)_S = (1.904 \pm 0.008, 19.618 \pm 0.006)$ derived from the measurements of CT13-I and V in the light-curve modeling, which is detailed in Appendix A. We also derived the source color and magnitude from the measurements of OGLE-I and V and confirmed that they are consistent within 2σ, which is also detailed in Appendix A. In addition, we independently measured the source color using a linear regression from CT13-I and V, $(V - I)_{CT13,reg} = 1.910 \pm 0.005$, which is consistent with $(V - I)_S$. Therefore, we determined that the measurements of the source color and magnitude are robust. Here, we took the source color and magnitude derived from the CT-13 measurements because both CT13-I and -V covered the light curve well when the primary source were significantly magnified.

Figure 7 shows the CMD of the OGLE-III catalog within 60′ of the sources plotted as black dots, and the CMD of Baade's window from Holtzman et al. (1998) plotted as green dots. We found that the extinction-free color and magnitude of the primary source star are $(V - I, I)_{S,0} = (0.582 \pm 0.071, 17.936 \pm 0.049)$ assuming that the source suffers from the same extinction of the RCG centroid of $(E(V - I), A_I)_{RCG} = (1.322 \pm 0.071, 1.682 \pm 0.049)$. The primary and secondary source stars are represented as the blue and magenta dots in Figure 7. The primary source star seems to be somewhat bluer and brighter than other typical bulge dwarfs, which implies that the source possibly suffered less from reddening and extinction than the bulge RCG centroid.

4.2. Spectroscopic Source Properties

Bensby et al. (2017) took a spectrum of OGLE-2013-BLG-0911S and reported the source properties in detail, which are summarized in Table 4.[79] They suggested a possibility that the source star belongs to the foreground Galactic disk for three reasons. First, they measured the lens-source relative proper motion of $\mu \sim 0.3$ mas yr^{-1} based on their single-lens microlensing model and indicated that this small value preferred the foreground disk source. Second, the intrinsic source color $(V - I)_{S,0} = 0.71^{+0.03}_{-0.02}$ based on their spectroscopic measurement is redder than $(V - I)_{S,0} = 0.49$ from their microlensing analysis, which implies that the source suffers less extinction than the average RCG in this field. They suggested that this may be because the source is in the foreground disk. Note that our derived $(V - I)_{S,0}$ assuming the source is behind all of the dust, is less blue (0.58 versus 0.49), but is still substantially bluer than Bensby's spectroscopic value. Third, they claimed that the heliocentric RV of the source, RV$_{helio}$, is consistent with a disk star.

However, if we adopt $I_{S,0} = 17.94$, which is derived from our light-curve modeling and the absolute source magnitude $M_I = 2.98$, which is estimated from spectroscopic values in Bensby et al. (2017), these measurements yield a source distance of ~ 9.8 kpc, which would put the source within or behind the bulge. Furthermore, we consider that the above rationale for the disk source scenario is not strong for three
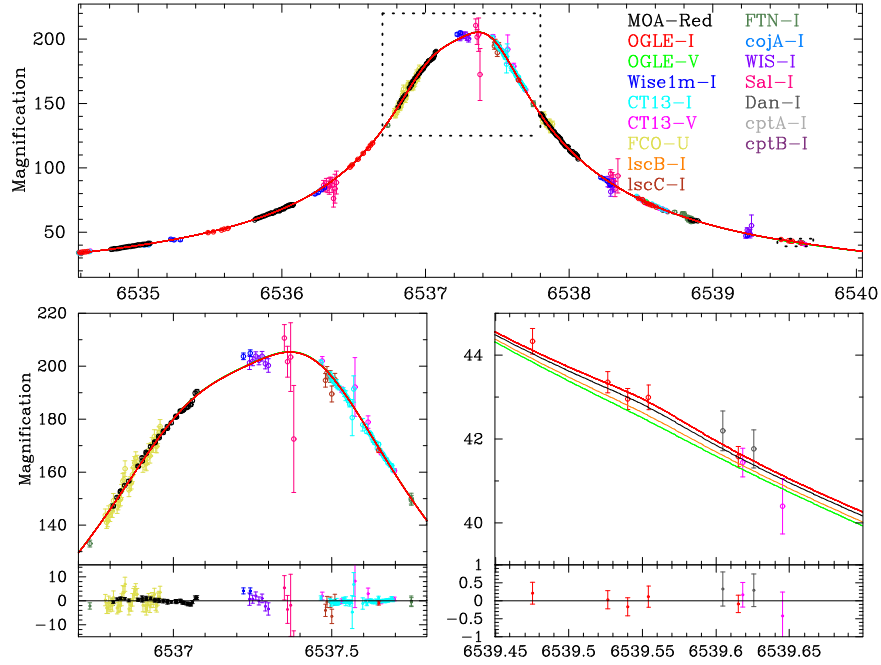

Figure 5. Light curve of OGLE-2013-BLG-0911. Each color on the data point corresponds to each instrument, shown on the right. The error bars are renormalized following Equation (1). The 2L2S ($s < 1$, $u_0 > 0$) model light curves in MOA–Red, I, V, Unfiltered bands are shown as the solid black, red, green, and orange lines, respectively. The dotted boxes in the top panel correspond to the areas represented in the bottom left and right panels, where the primary and secondary sources were significantly magnified, respectively.

reasons. First, both our 2L2S and 2L1S models provided $\mu \sim 3$ mas yr^{-1}, which does not strongly favor the foreground disk source. It is likely that their 1L1S model, which could not fit the light curve properly, derived the incorrect values of $\mu \sim 0.3$ mas yr^{-1} and $(V - I)_{S,0} = 0.49$. Second, the color of $(V - I)_{S,0} = 0.58 \pm 0.07$ derived in our analysis is between their spectroscopic and microlensing values, and we found a similar color with their microlensing value when we used RCGs in slightly wider areas around the target, where the RCG distribution gets spread wider along the extinction vector on the CMD. These indicate that their spectroscopic color $(V - I)_{S,0} = 0.71^{+0.03}_{-0.02}$ is correct as well as their and our photometric colors $(V - I)_{S,0} = 0.49$ and 0.58 ± 0.07, respectively, which are based on the average color of RCG in wider area, are biased because of low spatial resolution relative to the actual spatial variation of the reddening. Therefore, we conclude that the color difference may be due to the local spatial variation of the extinction in this field rather than the foreground disk scenario. Third, the constraint from RV$_{\mathrm{helio}}$ is not strong because it is also sufficiently explained by the bulge velocity distribution, which has a large dispersion of $\sigma \sim 100$ km s^{-1} (Howard et al. 2008).

Finally, we adopt 90% of the RCG extinction as the source extinction, i.e., $(E(V - I), A_I)_S = 0.9 \times (E(V - I), A_I)_{\mathrm{RCG}} = (1.190 \pm 0.064, 1.514 \pm 0.044)$ and thus the intrinsic primary source color and magnitude are $(V - I, I)_{S,0} = (0.714 \pm 0.071, 18.109 \pm 0.049)$. This is consistent with the spectroscopic source color $(V - I)_{S,0} = 0.71^{+0.03}_{-0.02}$. Note that even if we assumed that the source suffered from the same extinction as that for average RCG, the estimated source angular radius θ_* is consistent with that of 90% of the average RCG extinction. The source properties are summarized in Table 4.

Table 4
Source Properties

	$V - I$ (mag)	I (mag)	θ_* (μas)
Apparent	1.904 ± 0.009	19.618 ± 0.006	$\cdots$
Intrinsic	0.714 ± 0.071	18.104 ± 0.049	0.757 ± 0.054
From Bensby et al. (2017)			
Effective Temperature	T_{eff} [a]		5785 ± 77 (K)
	T_{eff} [b]		6616 (K)
Source Color	$(V - I)_{S,0}$ [a]		$0.71^{+0.03}_{-0.02}$ (mag)
	$(V - I)_{S,0}$ [b]		0.49 (mag)
Absolute Magnitude	M_V [a]		3.69 (mag)
Heliocentric RV	RV$_{\mathrm{helio}}$		-46.8 (km s^{-1})

Notes. Bensby et al. (2017) modeled OGLE-2013-BLG-0911 as a 1L1S event.
[a] Derived from spectroscopy.
[b] Derived from their microlensing model.

4.3. Angular Source and Einstein Radius

With the extinction-free color and magnitude of the source, we can estimate θ_* from a precise empirical $(V - I)$ and I relation

$$\log_{10}\left(\frac{2\theta_*}{\mathrm{mas}}\right) = 0.5014 + 0.4197(V - I)_{S,0} - 0.2I_{S,0}, \quad (8)$$

which is the optimized relation for the color ranges of microlensing observation, derived from the extended analysis of Boyajian et al. (2014). Using Equation (8), we estimated $\theta_* = 0.757 \pm 0.054$ μas for the best-fit model. We used Equation (8) and took account of the source extinction and its uncertainty into our MCMC calculations to derive the angular Einstein radius θ_E and the geocentric lens-source
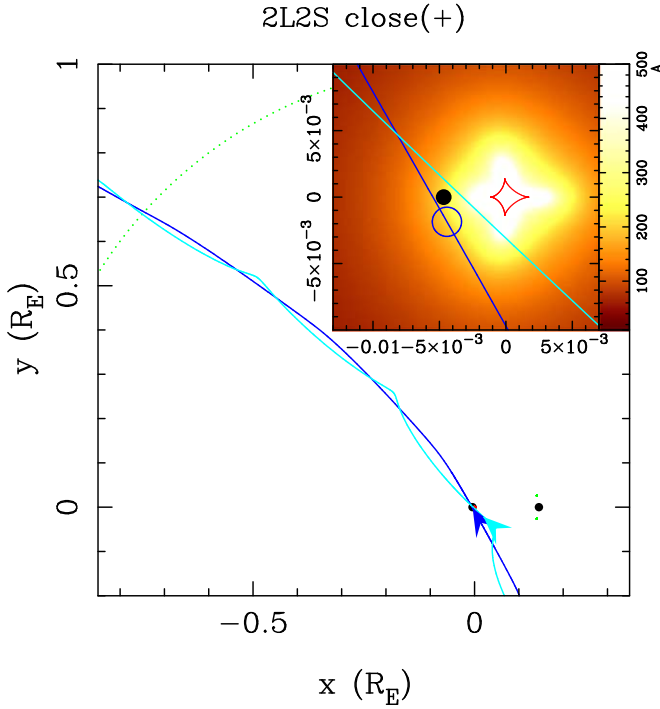
Figure 6. Caustic geometry for the best-fit 2L2S ($s < 1$, $u_0 > 0$) model is shown as the red curves, respectively. The blue and light blue curves show the primary and secondary source trajectories with respect to the lens systems, with the arrows indicating the directions of each source motion. The black dots are lens components, and the green dots represent critical curves. The inset shows a zoom-in view around the central caustic. The magnification patterns are described as color maps. The brighter tone denotes higher magnification. The blue circle on the lines indicates the primary source size and its positions is at t_0.

relative proper motion $\mu_{\rm rel,G}$ for each model. The results are summarized in Table 5.

5. Lens System Properties

The measurements of both $\theta_{\rm E}$ and $\pi_{\rm E}$ enable us to determine the lens mass M_L and distance D_L directly (Gould 2000; Bennett 2008) as follows:

$$M_L = \frac{c^2}{4G}\theta_{\rm E}^2\frac{D_S D_L}{D_S - D_L} = \frac{c^2}{4G}\frac{\rm au}{\pi_{\rm E}^2}\frac{D_S - D_L}{D_S D_L} = \frac{\theta_{\rm E}}{\kappa \pi_{\rm E}}, \quad (9)$$

where D_L is the lens distances. We derived the probability distributions of the physical parameters of the source and lens systems by calculating their values in each MCMC link. Here, we assumed the primary source mass $M_S = 1\,M_\odot$ and the source distance $D_S = 8$ kpc. As referred to in Appendix B, we confirmed that the assumptions hardly affect the MCMC posterior distributions for the lens physical parameters except for the lens distance D_L. We combined the posterior probability distributions of each model weighting by $e^{-\Delta\chi^2/2}$. Figure 8 shows the probability distributions of the lens mass M_L and distance D_L for the close and wide models, and the final result of the physical parameters are summarized in Table 5. The result indicates that the lens system is an M dwarf orbited by a massive Jupiter companion at very close ($M_{\rm host} = 0.30^{+0.08}_{-0.06}M_\odot$, $M_{\rm comp} = 10.1^{+2.9}_{-2.2}M_{\rm Jup}$, $a_{\rm exp} = 0.40^{+0.05}_{-0.04}$ au) or wide ($M_{\rm host} = 0.28^{+0.10}_{-0.08}M_\odot$, $M_{\rm comp} = 9.9^{+3.8}_{-3.5}M_{\rm Jup}$, $a_{\rm exp} = 18.0^{+3.2}_{-3.2}$ au) separation.
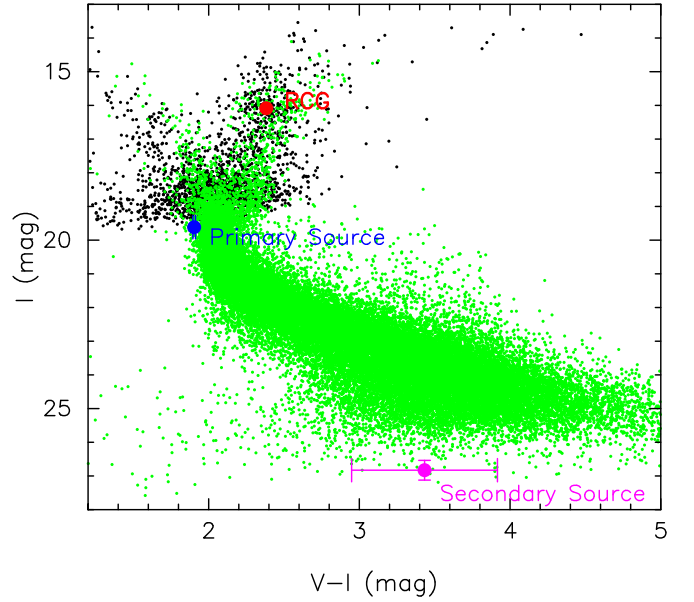

Figure 7. The $(V - I, I)$ CMD in the standard Kron–Cousins I and Johnson V photometric system. The positions of the primary and secondary source and the centroid of RCG are shown as the blue, magenta, and red circles. The black dots indicate the OGLE-III catalog stars within $1'$ of the source. The green dots indicate the *Hubble Space Telescope* (*HST*) CMD in Baade's window (Holtzman et al. 1998), whose color and magnitude are matched by using the RCG position.

Table 5
Physical Parameters

Parameters	Units	Close	Wide
Lens Host Mass, $M_{\rm host}$	$M_\odot$	$0.29^{+0.07}_{-0.05}$	$0.28^{+0.10}_{-0.08}$
Lens Companion Mass, $M_{\rm comp}$	$M_{\rm Jup}$	$9.51^{+2.72}_{-1.69}$	$9.92^{+3.78}_{-3.45}$
Lens Distance, D_L	kpc	$3.22^{+0.47}_{-0.35}$	$3.15^{+0.53}_{-0.42}$
Expected Semimajor Axis, $a_{\rm exp}$[a]	au	$0.39^{+0.05}_{-0.03}$	$17.98^{+3.21}_{-3.24}$
Source Companion Mass, M_C	$M_\odot$	$0.137^{+0.018}_{-0.016}$	$0.137^{+0.017}_{-0.014}$
Distance between Sources, $a_{\rm SC}$	au	$0.225^{+0.004}_{-0.004}$	$0.225^{+0.003}_{-0.003}$
Angular Einstein Radius, $\theta_{\rm E}$	mas	$0.67^{+0.10}_{-0.08}$	$0.68^{+0.14}_{-0.17}$
Geocentric Lens-Source Proper Motion, $\mu_{\rm rel,G}$	mas yr^{-1}	$2.54^{+0.37}_{-0.30}$	$2.50^{+0.56}_{-0.65}$
Predicted Lens Magnitude, V_L	mag	$26.42^{+1.15}_{-1.13}$	
Predicted Lens Magnitude, I_L	mag	$22.80^{+0.88}_{-0.83}$	
Predicted Lens Magnitude, H_L	mag	$19.99^{+0.79}_{-0.78}$	
Predicted Lens Magnitude, K_L	mag	$19.64^{+0.78}_{-0.76}$	

Notes. The median value and 68.3% confidence interval derived from MCMC. Here, we assume $D_S = 8$ kpc and $M_S = 1M_\odot$ except for the lens magnitudes.
[a] $a_{\rm exp} = \sqrt{3/2}\,a_\perp$.

We evaluated the expected apparent magnitude of the lens brightness by conducting a Bayesian analysis based on the observed $t_{\rm E}$, $\theta_{\rm E}$, and $\pi_{\rm E}$ and prior probabilities from a standard Galactic model (Sumi et al. 2011). Here, we evaluated the extinction in front of the lens given by

$$A_{i,L} = \frac{1 - e^{-D_L/h_{\rm dust}}}{1 - e^{-D_S/h_{\rm dust}}}A_{i,S}, \quad (10)$$

where the index i corresponds to the passband V, I, H, and K, and the $h_{\rm dust} = (0.1\ {\rm kpc})/\sin|b|$ is a scale length of the dust toward the event (Bennett et al. 2015). The lens brightness and
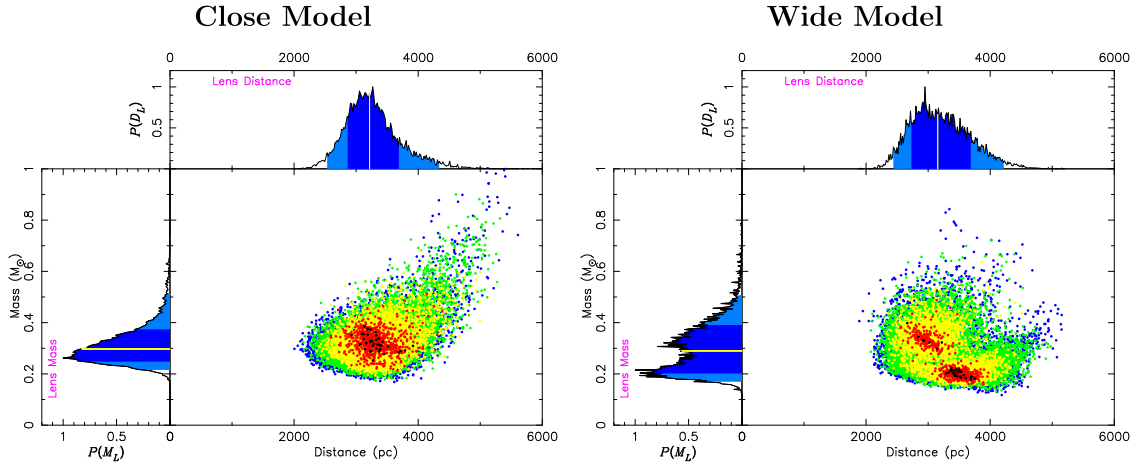
Close Model

Wide Model

Figure 8. The main panel shows the $\Delta\chi^2$ distribution of the lens mass M_L and distance D_L for the close and wide models derived from MCMC, where the black, red, yellow, green, and blue dots indicate links with $\Delta\chi^2 < 1, 4, 9, 16,$ and 25, respectively. The top and left insets represent the posterior probability distributions of M_L and D_L, where the dark and light blue regions indicate the 68.3% and 95.4% confidence intervals, and the perpendicular yellow lines indicate the median values.

the extinction values are estimated from the color–color and mass–luminosity relations of main-sequence stars (Henry & McCarthy 1993; Kenyon & Hartmann 1995; Kroupa & Tout 1997) and the extinction law in Nishiyama et al. (2009), respectively. We also estimated the source magnitudes in H- and K-bands from Kenyon & Hartmann (1995), taking into account a 10% uncertainty. Figure 9 represents the apparent lens magnitudes in each band derived from the Bayesian analysis. The dark and light blue regions indicate the 68.3% and 95.4% confidence intervals, and the vertical blue lines indicate the median values. The vertical solid and dashed red lines are the source magnitudes and their 1σ uncertainties in each passband. The relationship between the heliocentric and geocentric relative proper motion is

$$\boldsymbol{\mu}_{\rm rel,H} = \boldsymbol{\mu}_{\rm rel,G} + \frac{\pi_{\rm rel}}{\rm au}\boldsymbol{v}_\oplus \qquad (11)$$

where $\pi_{\rm rel} = {\rm au}(D_L^{-1} - D_S^{-1})$ and $\boldsymbol{v}_\oplus = (v_{\oplus,N}, v_{\oplus,E}) = (-2.91, 9.44)$ km s^{-1} are the relative lens-source parallax and the instant velocity of Earth on the plane of the sky at the reference time, respectively. The heliocentric relative proper motion is $\mu_{\rm rel,H} \sim 2.5$ mas yr^{-1}, and thus, the angular separation between the source and lens would be ~ 15 mas in 2019. Bhattacharya et al. (2017) have demonstrated the feasibility of *HST* follow-up observations to measure the separation between the source and the lens with 12 mas when the lens is not too much fainter than the source. (The current state of technical arts for high angular resolution analysis is detailed in Bhattacharya et al. 2018.) Hence, it might benefit from a high-resolution follow-up observation in order to constrain the physical parameters of the lens system. However, we note that the four degenerate solutions have parallax vectors $\boldsymbol{\pi}_E$ with amplitudes, directions, and uncertainties approximately similar to each other, and thus, it is unlikely that the degenerate solutions are resolved by high-resolution follow-up observations.

6. Summary and Discussion

We have presented our analysis of the microlensing event OGLE-2013-BLG-0911. Previous research on the event
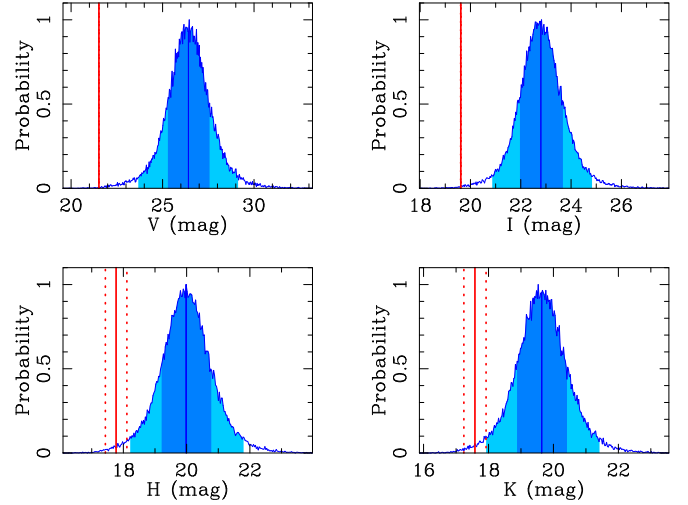

Figure 9. Posterior probabilities of the lens apparent magnitudes derived from the Bayesian analysis with the observed t_E, θ_E, and π_E and prior probabilities from a standard Galactic model. The dark and light blue regions indicate the 68.3% and 95.4% confidence intervals, and the perpendicular blue lines indicate the median values. The vertical solid and dashed red lines are the source magnitudes and their 1σ uncertainties in each passband.

(Shvartzvald et al. 2016) reported that the lensing anomaly could be explained by a planetary mass ratio, $q \approx 3 \times 10^{-4}$. From a detailed grid search analysis, however, we found that a binary mass ratio $q \approx 3 \times 10^{-2}$ is preferred over a planetary mass ratio to explain the light curve. Finally, we conclude that the lens system consists of an M dwarf orbited by a massive Jupiter companion at very close ($M_{\rm host} = 0.30^{+0.08}_{-0.06}M_\odot$, $M_{\rm comp} = 10.1^{+2.9}_{-2.2}M_{\rm Jup}$, $a_{\rm exp} = 0.40^{+0.05}_{-0.04}$ au) or wide ($M_{\rm host} = 0.28^{+0.10}_{-0.08}M_\odot$, $M_{\rm comp} = 9.9^{+3.8}_{-3.5}M_{\rm Jup}$, $a_{\rm exp} = 18.0^{+3.2}_{-3.2}$ au) separation.

Microlensing light curves generally provide much more precise estimation of the mass ratio than that of the absolute lens mass. Bond et al. (2004) defined the mass ratio boundary between BDs and planets as $q = 0.03$ in order to distinguish between planetary and stellar binary (including BD) microlensing events. For this event, the best-fit mass ratio is slightly above the mass ratio boundary of $q = 0.03$. On the other hand, the median mass of the companion is slightly below the lower limit of the BD mass of $13M_{\rm Jup}$. Therefore, it is ambiguous to

classify the companion as a BD or a planet. In fact, these boundaries are somewhat arbitrary, and it might be nonsense to classify such an ambiguous companion according to the boundaries. However, the formation mechanisms for BDs and planets are likely to be different, and the object near the boundaries could have been formed by either formation mechanism. Therefore, it would be very important to probe the distribution of intermediate-mass companions of $\sim 13 M_{\rm Jup}$.

Missing the best lens model explanation to the observed microlensing light-curve data might have serious impacts on any statistical microlensing analysis incorporating those modeling results. For instance, Shvartzvald et al. (2016) suggests that there is a possible BD deficit corresponding to $q \sim 10^{-2}$ in their detection-efficiency-corrected mass ratio function. However, we found OGLE-2013-BLG-0911, which was adopted as a planetary sample in their analysis, would correspond to the position of the BD deficit, which would affect their result to some extent. The reason why they missed the best solution would be the very small/wide projected separation $s \approx 0.2$ or ≈ 7. They explored the s parameter space of $0.3 < s < 3$ in their grid search analysis. It is known that a central caustic size is approximately proportional to not only q but also s^2 (for $s \ll 1$) and s^{-2} (for $s \gg 1$) (Chung et al. 2005). Therefore, when we model microlensing light curves with perturbations caused by possibly small-size central caustics, we should suspect the possibilities of not only very low-mass but also very close and wide-lens companions. The detection efficiency for companions with such extremely close and wide separation is much lower than that with $s \approx 1$ (Suzuki et al. 2016). Hence, even a small number of detections may be important in the statistical analysis.

The successful discovery of the best-fit model depends on the initial parameters for the MCMC fitting. Currently, the initial parameters for modeling binary-lens events are mainly based on the experiences of the modelers or the brute-force of the grid search analysis across a wide range of parameter spaces. The systematic analysis of many events relies on the latter method. However, it would not work if the best-fit solutions are out of range of the grid search, which happened on this event OGLE-2013-BLG-0911. Broadening the search range as possible is a straightforward way to avoid the problem. However, it is computationally expensive and getting more difficult for statistical analysis, including hundreds of stellar binary events in the recent high-cadence surveys by MOA, OGLE, and KMTNet (Kim et al. 2016). Furthermore, the *Wide Field Infrared Survey Telescope* (Spergel et al. 2015) will be launched in 2025 and is expected to discover $\sim 54,000$ microlensing events ($|u_0| < 3$) with thousands of binary-lens events, including ~ 1400 bound exoplanets with masses of $0.1 < M_p/M_\oplus < 10^4$ (Penny et al. 2019). We should consider a new method to efficiently search for the best binary-lens solutions. Bennett et al. (2012) applied a different parameterization for wide-separate binary events. Khakpash et al. (2019) proposed an algorithm that can rapidly evaluate many binary-lens light curves and estimate the physical parameters of the lens systems, which is successful for very low-mass-ratio events but less so for higher mass-ratio events.

There are only four discoveries of BD companions to M dwarfs within 10 pc from solar system (Winters et al. 2018), while approximately 200 M dwarfs are known to exist within 10 pc (Henry et al. 2006, 2016) and much effort has been dedicated to detect such BD companions (Henry & McCarthy 1990;

Dieterich et al. 2012). Because of their scarcity, incoming new BD discoveries around M dwarfs provide valuable constraints on the formation and evolution theories of stars, BDs, and planets. Microlensing is a powerful method to probe the BD/massive-planet occurrence frequency across orbital radii $0.1 \leqslant a \leqslant 10$ au around low-mass hosts such as M dwarfs and even BDs (Gaudi 2002), which is challenging for other exoplanet detection methods. Although microlensing samples generally cannot provide some information such as host metallicity and eccentricity, microlensing can provide both their masses and orbital separations. It is very important to uncover the distributions of BD properties by microlensing.

Appendix A
Calibration for the Source Magnitude

We derived the apparent magnitude and color of the source from the measurements of CT13-I and V that were made during the time of high magnification. We basically followed the procedure described in Bond et al. (2017) in order to convert the CT13 instrumental magnitudes into the standard ones. We cross-referenced isolated stars around $2'$ of the source between the CT13 catalog reduced by DoPHOT (Schechter et al. 1993) and the OGLE-III catalog (Szymański et al. 2011). We found the following relation:

$$I_{\rm O3} - I_{\rm CT13} = (27.070 \pm 0.011) - (0.032 \pm 0.006)(V-I)_{\rm CT13}$$
$$V_{\rm O3} - V_{\rm CT13} = (27.851 \pm 0.017) - (0.101 \pm 0.011)(V-I)_{\rm CT13}.$$

Consequently, we obtained the apparent color and magnitude of the source, $(V-I, I)_{S,\rm CT13} = (1.904 \pm 0.009, 19.618 \pm 0.006)$. Moreover, we also derived the source color and magnitude from
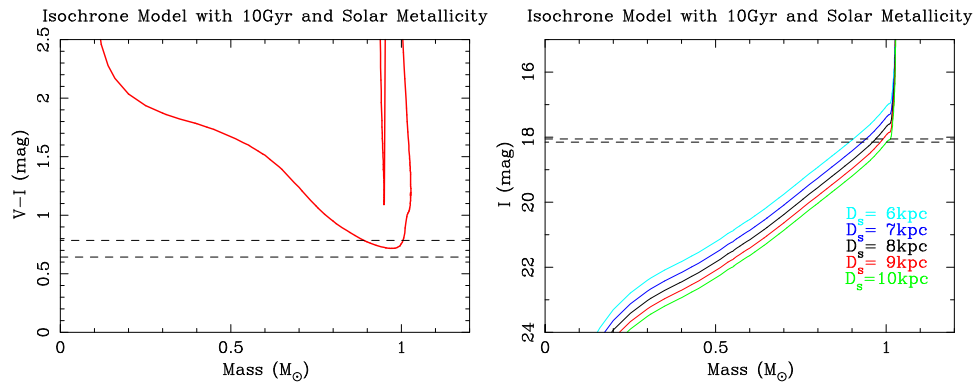
Figure 10. PARSEC stellar isochrone model with solar metallicity and 10 Gyr age. The areas enclosed by the horizontal dashed lines represent the 1σ ranges for the observed intrinsic source color $(V - I)_{S,0} = 0.714 \pm 0.071$ (right panel) and magnitude $I_{S,0} = 18.104 \pm 0.049$ (left panel), respectively.

the measurements of OGLE-I and V for confirmation. We used Equation (1) in Udalski et al. (2015) to calibrate the OGLE-IV instrumental magnitudes into the standard ones. We applied $\Delta ZP_I = -0.056$, $\Delta ZP_V = 0.133$, $\epsilon_I = -0.005 \pm 0.003$, and $\epsilon_V = -0.077 \pm 0.001$ for Equation (1) in Udalski et al. (2015), which were obtained by private communication with the OGLE collaboration. Finally, we derived the apparent source color and magnitude from OGLE-I and V, $(V - I, I)_{S,O4} = (1.880 \pm 0.009, 19.594 \pm 0.006)$.

Appendix B
Impact of the Assumption for M_S and D_S

We tested how the assumption of the fixed $M_S = 1\,M_\odot$ and $D_S = 8$ kpc impacted the final results. Figure 10 represents the PARSEC stellar isochrone with solar metallicity and 10 Gyr age. Comparing the isochrone to the observed intrinsic source color and magnitude $(V - I, I)_{S,0} = (0.714 \pm 0.071, 18.104 \pm 0.049)$, we can state that the source mass and distance are likely to be in the ranges of $0.9 \leqslant M_S/M_\odot \leqslant 1.0$ and $6\,\mathrm{kpc} \leqslant D_S \leqslant 10\,\mathrm{kpc}$, respectively. In these likely ranges, we conducted light-curve modeling for 1L2S, 2L1S, and 2L2S with all 15 combinations of the fixed $M_S = (0.9, 0.95, 1.0)\,M_\odot$ and $D_S = (6, 7, 8, 9, 10)$ kpc. We found that the fixed values have little effect on the best-fit χ^2 value, and the MCMC posterior distributions for the lens physical parameters are consistent with each other within 1σ except for the lens distance D_L. Therefore, we conclude that the assumptions for M_S and D_S do not significantly affect the final results except D_L.

ORCID iDs

Shota Miyazaki ⓘ https://orcid.org/0000-0001-9818-1513
David P. Bennett ⓘ https://orcid.org/0000-0001-8043-8413
Yossi Shvartzvald ⓘ https://orcid.org/0000-0003-1525-5041
Valerio Bozza ⓘ https://orcid.org/0000-0003-4590-0136
Jennifer C. Yee ⓘ https://orcid.org/0000-0001-9481-7123
Nicholas Rattenbury ⓘ https://orcid.org/0000-0001-5069-319X
Naoki Koshimoto ⓘ https://orcid.org/0000-0003-2302-9562
Akihiko Fukui ⓘ https://orcid.org/0000-0002-4909-5763 and
Y. Itow ⓘ https://orcid.org/0000-0002-8198-1968
I. Kondo ⓘ https://orcid.org/0000-0002-3401-1029
J. Skowron ⓘ https://orcid.org/0000-0002-2335-1730
P. Pietrukowicz ⓘ https://orcid.org/0000-0002-2339-5899
K. Ulaczyk ⓘ https://orcid.org/0000-0001-6364-408X
M. Albrow ⓘ https://orcid.org/0000-0003-3316-4012
A. Gal-Yam ⓘ https://orcid.org/0000-0002-3653-5598
R. W. Pogge ⓘ https://orcid.org/0000-0003-1435-3053
Y. Tsapras ⓘ https://orcid.org/0000-0001-8411-351X
E. Bachelet ⓘ https://orcid.org/0000-0002-6578-5078
K. Horne ⓘ https://orcid.org/0000-0003-1728-0304
C. Snodgrass ⓘ https://orcid.org/0000-0001-9328-2905
J. Wambsganss ⓘ https://orcid.org/0000-0002-8365-7619
I. A. Steele ⓘ https://orcid.org/0000-0001-8397-5759
G. D'Ago ⓘ https://orcid.org/0000-0001-9697-7331
T. C. Hinse ⓘ https://orcid.org/0000-0001-8870-3146
N. Kains ⓘ https://orcid.org/0000-0001-8803-6769
L. Mancini ⓘ https://orcid.org/0000-0002-9428-8732
M. Rabus ⓘ https://orcid.org/0000-0003-2935-7196
S. Rahvar ⓘ https://orcid.org/0000-0002-7084-5725
N. Peixinho ⓘ https://orcid.org/0000-0002-6830-476X

References

Alard, C. 2000, A&AS, 144, 363
Alard, C., & Lupton, R. H. 1998, ApJ, 503, 325
Albrow, M. D., Horne, K., Bramich, D. M., et al. 2009, MNRAS, 397, 2099
André, P., Ward-Thompson, D., & Greaves, J. 2012, Sci, 337, 69
Armitage, P. J., & Bonnell, I. A. 2002, MNRAS, 330, L11
Batista, V., Dong, S., Gould, A., et al. 2009, A&A, 508, 467
Bennett, D. P. 2008, in Exoplanets, ed. J. W. Mason (Berlin: Springer), 47
Bennett, D. P. 2010, ApJ, 716, 1408
Bennett, D. P., Batista, V., Bond, I. A., et al. 2014, ApJ, 785, 155
Bennett, D. P., Bhattacharya, A., Anderson, J., et al. 2015, ApJ, 808, 169
Bennett, D. P., Bond, I. A., Udalski, A., et al. 2008, ApJ, 684, 663
Bennett, D. P., & Rhie, S. H. 1996, ApJ, 472, 660
Bennett, D. P., Sumi, T., Bond, I. A., et al. 2012, ApJ, 757, 119
Bennett, D. P., Udalski, A., Han, C., et al. 2018, AJ, 155, 141
Bensby, T., Adén, D., Meléndez, J., et al. 2011, A&A, 533, A134
Bensby, T., Feltzing, S., Gould, A., et al. 2017, A&A, 605, A89
Bensby, T., Yee, J. C., Feltzing, S., et al. 2013, A&A, 549, A147
Bhattacharya, A., Beaulieu, J.-P., Bennett, D. P., et al. 2018, AJ, 156, 289
Bhattacharya, A., Bennett, D. P., Anderson, J., et al. 2017, AJ, 154, 59
Bond, I. A., Abe, F., Dodd, R. J., et al. 2001, MNRAS, 327, 868
Bond, I. A., Bennett, D. P., Sumi, T., et al. 2017, MNRAS, 469, 2434
Bond, I. A., Udalski, A., Jaroszyński, M., et al. 2004, ApJL, 606, L155
Borucki, W. J., Koch, D., Basri, G., et al. 2010, Sci, 327, 977
Boss, A. P. 1997, Sci, 276, 1836
Boss, A. P. 2001, ApJL, 551, L167
Boyajian, T. S., van Belle, G., & von Braun, K. 2014, AJ, 147, 47
Bramich, D. M. 2008, MNRAS, 386, L77
Bramich, D. M., Horne, K., Albrow, M. D., et al. 2013, MNRAS, 428, 2275
Bressan, A., Marigo, P., Girardi, L., et al. 2012, MNRAS, 427, 127
Burrows, A., Hubbard, W. B., Saumon, D., & Lunine, J. I. 1993, ApJ, 406, 158
Carnero Rosell, A., Santiago, B., & dal Ponte, M. 2019, MNRAS, 489, 5301
Choi, J.-Y., Shin, I.-G., Han, C., et al. 2012, ApJ, 756, 48

Chung, S.-J., Han, C., Park, B.-G., et al. 2005, ApJ, 630, 535
Claret, A., & Bloemen, S. 2011, A&A, 529, A75
Dieterich, S. B., Henry, T. J., Golimowski, D. A., Krist, J. E., & Tanner, A. M. 2012, AJ, 144, 64
Dominik, M. 1999, A&A, 349, 108
Dominik, M., Bachelet, E., Bozza, V., et al. 2019, MNRAS, 484, 5608
Dominik, M., Jørgensen, U. G., Rattenbury, N. J., et al. 2010, AN, 331, 671
Duchêne, G., & Kraus, A. 2013, ARA&A, 51, 269
Gaudi, B. S. 1998, ApJ, 506, 533
Gaudi, B. S. 2002, arXiv:astro-ph/0206494
Gaudi, B. S., Beaulieu, J. P., Bennett, D. P., et al. 2009, astro2010: The Astronomy and Astrophysics Decadal Survey, Science White Papers, 85
González Hernández, J. I., & Bonifacio, P. 2009, A&A, 497, 497
Gorbikov, E., Brosch, N., & Afonso, C. 2010, Ap&SS, 326, 203
Gould, A. 1992, ApJ, 392, 442
Gould, A. 2000, ApJ, 542, 785
Gould, A. 2004, ApJ, 606, 319
Gould, A., Dong, S., Bennett, D. P., et al. 2010, ApJ, 710, 1800
Gould, A., Udalski, A., An, D., et al. 2006, ApJL, 644, L37
Gould, A., & Welch, D. L. 1996, ApJ, 464, 212
Grether, D., & Lineweaver, C. H. 2006, ApJ, 640, 1051
Griest, K., & Hu, W. 1992, ApJ, 397, 362
Griest, K., & Safizadeh, N. 1998, ApJ, 500, 37
Han, C., & Gould, A. 1997, ApJ, 480, 196
Han, C., Udalski, A., Sumi, T., et al. 2017, ApJ, 843, 59
Hayashi, C. 1981, in Fundamental Problems in the Theory of Stellar Evolution, ed. D. Sugimoto, D. Q. Lamb, & D. N. Schramm (Dordrecht: D. Reidel), 113
Henry, T. J., Jao, W.-C., Subasavage, J. P., et al. 2006, AJ, 132, 2360
Henry, T. J., Jao, W.-C., Winters, J. G., et al. 2016, AAS Meeting Abstracts, 227, 142.01
Henry, T. J., & McCarthy, D. W., Jr. 1990, ApJ, 350, 334
Henry, T. J., & McCarthy, D. W., Jr. 1993, AJ, 106, 773
Holtzman, J. A., Watson, A. M., Baum, W. A., et al. 1998, AJ, 115, 1946
Howard, C. D., Rich, R. M., Reitzel, D. B., et al. 2008, ApJ, 688, 1060
Ida, S., & Lin, D. N. C. 2005, ApJ, 626, 1045
Johnson, J. A., Howard, A. W., Marcy, G. W., et al. 2010, PASP, 122, 149
Jung, Y. K., Udalski, A., Bond, I. A., et al. 2017a, ApJ, 841, 75
Jung, Y. K., Udalski, A., Yee, J. C., et al. 2017b, AJ, 153, 129
Kenyon, S. J., & Hartmann, L. 1995, ApJS, 101, 117
Khakpash, S., Penny, M., & Pepper, J. 2019, AJ, 158, 9
Kim, S.-L., Lee, C.-U., Park, B.-G., et al. 2016, JKAS, 49, 37
Kroupa, P., & Tout, C. A. 1997, MNRAS, 287, 402
Kumar, S. S. 1962, Institute for Space Studies Report No. X-644-62-78
Laughlin, G., Bodenheimer, P., & Adams, F. C. 2004, ApJL, 612, L73
Lissauer, J. J. 1993, ARA&A, 31, 129
Loeb, A., & Sasselov, D. 1995, ApJL, 449, L33
Luhman, K. L. 2012, ARA&A, 50, 65
Mao, S., & Paczynski, B. 1991, ApJL, 374, L37
Marcy, G. W., & Butler, R. P. 2000, PASP, 112, 137
Matzner, C. D., & Levin, Y. 2005, ApJ, 628, 817
Miyazaki, S., Sumi, T., Bennett, D. P., et al. 2018, AJ, 156, 136
Mordasini, C., Alibert, Y., Benz, W., & Naef, D. 2009, A&A, 501, 1161
Nakajima, T., Oppenheimer, B. R., Kulkarni, S. R., et al. 1995, Natur, 378, 463
Nataf, D. M., Gould, A., Fouqué, P., et al. 2013, ApJ, 769, 88
Nishiyama, S., Tamura, M., Hatano, H., et al. 2009, ApJ, 696, 1407
Paczynski, B. 1986, ApJ, 304, 1
Penny, M. T., Gaudi, B. S., Kerins, E., et al. 2019, ApJS, 241, 3
Poindexter, S., Afonso, C., Bennett, D. P., et al. 2005, ApJ, 633, 914
Pollack, J. B., Hubickyj, O., Bodenheimer, P., et al. 1996, Icar, 124, 62
Ranc, C., Cassan, A., Albrow, M. D., et al. 2015, A&A, 580, A125
Rattenbury, N. J., Bond, I. A., Skuljan, J., & Yock, P. C. M. 2002, MNRAS, 335, 159
Ryu, Y.-H., Yee, J. C., Udalski, A., et al. 2018, AJ, 155, 40
Sako, T., Sekiguchi, T., Sasaki, M., et al. 2008, ExA, 22, 51
Schechter, P. L., Mateo, M., & Saha, A. 1993, PASP, 105, 1342
Shin, I.-G., Yee, J. C., Gould, A., et al. 2019, AJ, 158, 199
Shvartzvald, Y., & Maoz, D. 2012, MNRAS, 419, 3631
Shvartzvald, Y., Maoz, D., Udalski, A., et al. 2016, MNRAS, 457, 4089
Skowron, J., Udalski, A., Gould, A., et al. 2011, ApJ, 738, 87
Skowron, J., Udalski, A., Kozłowski, S., et al. 2016, AcA, 66, 1
Smith, M. C., Mao, S., & Paczyński, B. 2003, MNRAS, 339, 925
Spergel, D., Gehrels, N., Baltay, C., et al. 2015, arXiv:1503.03757
Sumi, T., Abe, F., Bond, I. A., et al. 2003, ApJ, 591, 204
Sumi, T., Kamiya, K., Bennett, D. P., et al. 2011, Natur, 473, 349
Suzuki, D., Bennett, D. P., Sumi, T., et al. 2016, ApJ, 833, 145
Szymański, M. K., Udalski, A., Soszyński, I., et al. 2011, AcA, 61, 83
Tanigawa, T., & Tanaka, H. 2016, ApJ, 823, 48
Tsapras, Y., Street, R., Horne, K., et al. 2009, AN, 330, 4
Udalski, A., Szymanski, M., Stanek, K. Z., et al. 1994, AcA, 44, 165
Udalski, A., Szymański, M. K., & Szymański, G. 2015, AcA, 65, 1
Verde, L., Peiris, H. V., Spergel, D. N., et al. 2003, ApJS, 148, 195
Winters, J. G., Irwin, J., Newton, E. R., et al. 2018, AJ, 155, 125
Wozniak, P. R. 2000, AcA, 50, 421
Yee, J. C., Shvartzvald, Y., Gal-Yam, A., et al. 2012, ApJ, 755, 102
Yoo, J., DePoy, D. L., Gal-Yam, A., et al. 2004, ApJ, 603, 139